Thermodynamic and stoichiometric constraint-based inference of metabolic phenotypes

Leupold, Karl Ernst Simeon

Chapter 4

Saccharomyces cerevisiae goes through distinct metabolic phases during its replicative lifespan

Simeon Leupold*, Georg Hubmann*, Athanasios Litsios, Anne C. Meinema, Alexandros Papagiannakis, Bastian Niebel, Georges Janssens, David Siegel and Matthias Heinemann

* These authors contributed equally to this work

(s*ubmitted*)

Author Contributions
GH, AM and MH conceived the idea of the study. GH, SL, AM and MH designed the study with input from BN. GH, AM and GJ performed the aging cultivation experiments. DS performed the metabolomics analysis. AL and AP performed the single cell analysis and batch cultivation experiments. GH developed the model to deconvolve the experimental data. SL developed the model to estimate intracellular fluxes. SL and GH analyzed experimental data. SL, GH and MH wrote the manuscript. MH supervised the study.

ABSTRACT

A comprehensive description of the phenotypic changes during cellular aging is key towards unraveling its causal forces. Using recently developed experimental tools and model-based inference methods, here, we generated a comprehensive account of the metabolic changes during the entire replicative life of *Saccharomyces cerevisiae*. With age, we found decreasing metabolite levels, decreasing growth and substrate uptake rates accompanied by a switch from aerobic fermentation to a respiratory metabolism, with increased glycerol and acetate production. The identification of intracellular metabolic fluxes revealed an increase in redox cofactor turnover, likely to combat the increased production of reactive oxygen species. The identified metabolic changes possibly reflect a dynamic adaptation to the age-associated, non-homeostatic increase in cell volume. With metabolism being an important factor of the cellular phenotype, this work complements our recent mapping of the transcriptomic and proteomic changes towards a holistic description of the cellular processes during aging.

INTRODUCTION

Cellular aging is a complex multifactorial process affected by an intertwined network of effectors such as protein translation, protein quality control, mitochondrial dysfunction and metabolism (1–4). Disentangling cause and effect is a major challenge in aging research (5). A key requisite towards unraveling the causal forces of cellular aging is a comprehensive account of the concomitant phenotypic changes. In the replicatively aging budding yeast *Saccharomyces cerevisiae*, a common model for mitotic aging (6), unfortunately, the application of cell ensemble-based omics methods has been difficult due to the rapid outgrowth of aging mother cells by the newly formed daughter cells. Through a novel cultivation technique, allowing us to generate large amounts of aged cells, we could recently perform proteome and transcriptome profiling throughout the whole lifespan of *S. cerevisiae*. There, on the basis of an identified gradually increasing uncoupling between protein and transcript levels of biogenesis-related genes, we conjectured that this uncoupling is one of the causal forces of aging (7). Furthermore, we found changes in metabolic protein expression and, consistent with an earlier report (8), in metabolic gene expression, suggesting an altered metabolism with increasing replicative age. Here, exploiting the novel cultivation technique, metabolomics and model-based inference methods (9), we identified a metabolic shift during the replicative lifespan of *S. cerevisiae*. With this work, we complement our recent proteome and transcriptome profiling data with the corresponding metabolome, and generate a description of the functional phenotypic changes accompanied with cellular aging which ultimately lead to senescence and cell cycle arrest.

RESULTS

Column-based cultivation to enrich aged mother cells

To generate large quantities of aged cells, required for the metabolic profiling, we used our earlier developed column-based cultivation technique. Here, biotinylated cells attached to streptavidin-conjugated iron beads are immobilized inside a column positioned in the center of a ring magnet. A continuous nutrient flow through the column removes emerging daughter cells, while largely retaining mother cells (Method 1) (7). Several columns operated in parallel, allowed harvesting cells at different time points, corresponding to cell age. At each harvesting, we obtained three samples differently enriched with aged mother cells; (1) from the column effluent, (2) from the column after an additional washing step, and (3) from the washing solution (in the following referred to as mix 1, 2 and 3) (Fig. 1). The exact sample composition (i.e. the fraction of mother, daughter and dead cells) was determined by flow cytometry using a combined dye-staining of propidium iodide and avidin–FITC. We then acquired the cell population-aver-

aged intracellular metabolite concentrations and, to assess physiological parameters, measured the change in extracellular metabolites due to cell growth over a period of 3 h. To infer the aged mother cells' metabolite levels, physiological parameters and intracellular metabolic fluxes from the mixed-sample measurements, we employed different mathematical model-based methods (Fig. 1).

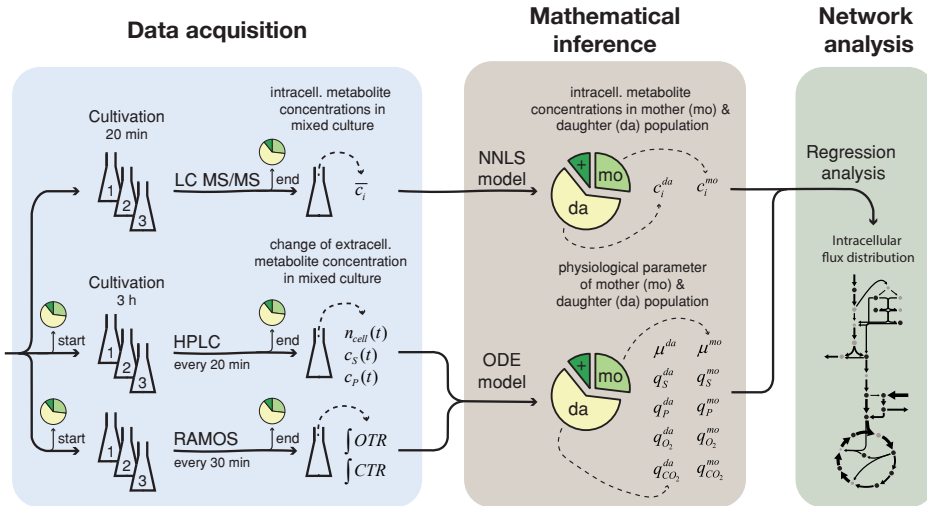

Figure 1 | Overview of the experimental and model-based analyses to determine the metabolite levels, physiological parameters and intracellular metabolic fluxes of replicatively aging budding yeast. Samples were harvested at various time points (corresponding to different cell ages) from a column-based cultivation system (7), designed to enrich aged mother cells. The fractional abundance of mother, daughter and dead cells in each sample was determined by flow cytometry and a combined dye-staining of propidium iodide and avidin–FITC. Aliquots were used to determine the intracellular metabolite concentrations, $\bar{c}_i$, by LC-MS/MS and the cell count, $n_{cell}(t)$, by flow cytometry, extracellular metabolites (i.e. substrates and products), $c_S(t)$ and $c_P(t)$, by HPLC and the integral of oxygen and carbon transfer rates, *OTR* and *CTR* (i.e. total consumed oxygen and produced carbon dioxide) by a Respiration Activity Monitoring System (RAMOS), in the mixed population samples. Next, the age-dependent intracellular metabolite concentrations (c_i) were inferred from the acquired population-average data using non-negative least square regression (NNLS) and the physiological parameters (growth (μ) and metabolite exchange rates (q)) of mother (*mo*) and daughter (*da*) cells) from an ordinary differential equation (ODE) model. The inferred physiological parameters and intracellular metabolite levels of aged mother cells were then analyzed using a combined stoichiometric-thermodynamic metabolic model and regression analyses to obtain the intracellular metabolic flux distribution.

Intracellular metabolite concentrations decrease with proceeding cell age

The intracellular concentrations of 18 metabolites were quantified by LC-MS/MS in the differently mixed samples (i.e. mix 1, 2 and 3), taken at various time points (after 10, 20, 44 and 68 h). As these concentration measurements resembled the average concentration of metabolites originating from mother and daughter cells, we used non-negative linear regression to infer the metabolite concentration in each individual population, using the determined fractional abundances of each population and the age-dependent cell volumes, which we determined with

microfluidics and microscopy (Method 2 and 5 and Supplementary Fig. 1). To confirm the validity of the regression approach, where in general a good fitting was achieved ($R^2 = 0.89$) (Supplementary Fig. 2a), we compared the concentrations for daughter cells, inferred from the mixed population samples, with metabolite concentrations determined from young streptavidin-labeled cells. Here, we found an excellent agreement ($R^2 = 0.99$) (Supplementary Fig. 2b).

Focusing on the intracellular metabolite dynamics in aging mother cells, we found that the concentrations of all quantified metabolites on average decreased to about 25 % of their initial values (Fig. 2a and Supplementary Fig. 2c). Remarkably, despite the drop in ATP levels, the adenylate energy charge was maintained between 0.8 and 0.95 (Supplementary Fig. 3), which corresponds to values of exponentially growing cultures (10). The drop in metabolic concentrations suggests that metabolic activities are globally decreased in aged cells and, as many metabolites have also regulatory function (11,12), the observed concentration changes are expected to lead to metabolic rearrangements.

Cells switch from a fermentative to a respiratory metabolism with age

To assess changes on the level of metabolic fluxes, we next determined the physiological rates, i.e. growth, metabolite uptake and excretion rates of aging cells. At each time point (after 10, 20, 44 and 68 h), we measured the evolution of cell count and extracellular concentrations of glucose, pyruvate, acetate, glycerol and ethanol over a period of three hours in each harvested sample (i.e. mix 1, 2 and 3). The fractional abundance of each cell population was determined before and after that period. We used a second set of aliquots to measure the evolution of produced carbon dioxide and consumed oxygen using a Respiration Activity Monitoring System (RAMOS) (13). To infer the population-specific physiological rates from the mixed-population samples, we fitted the acquired dynamic data to an ordinary differential equation model, describing the changes of the biomass and extracellular metabolite concentrations in the samples, due to mother and daughter cell growth and their respective metabolism (Method 3 and Supplementary Fig. 4). To assess the validity of the inference approach, we compared the physiological rates inferred for daughter cells to physiological rates obtained from unlabeled as well as from streptavidin-labeled cell cultures, both consisting of predominantly young cells. Here, we found a good agreement between the rates inferred for daughter cells and the rates obtained for both cultures containing young cells (Fig. 2b).

In aging cells, we found that the specific glucose uptake rate decreased drastically towards the end of their lifespan to almost 10 % of the value of young cells (Fig. 2b). This decrease was accompanied by a reduction of the growth rate, which we confirmed with single-cell measurements (Supplementary Fig. 5). Furthermore, while at a young age, cells showed a fermentative metabolic phenotype indicated by ethanol production and a low oxygen uptake rate (although oxygen

was sufficiently available in the setup (7)), with increasing age cells shifted towards a respiratory phenotype as indicated by an increase in oxygen uptake and reduced ethanol excretion (Fig. 2b). However, unlike a normal respiratory metabolism, where no byproducts would be excreted, up to half of the carbon influx was directed to glycerol and acetate excretion. The production of glycerol indicates a stress response (14) and acetate metabolism was linked to apoptosis (15). At the end of their lifespan (starting from time point 44 h), cells started to co-consume ethanol, produced by surrounding daughter cells. The identified stress responsive metabolism and decreased glucose uptake rate are consistent with signatures related to starvation and oxidative stress, as determined in our earlier proteome and transcriptome analysis (7).

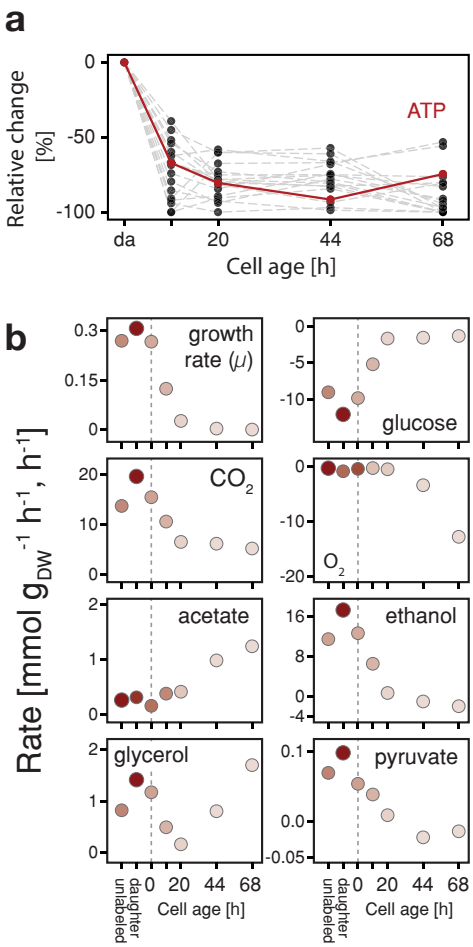

Figure 2 | Changes in metabolite concentrations and physiological parameters during cellular aging. (a) The intracellular metabolite concentrations of 18 metabolites at various cell ages were inferred from LC-MS/MS measurements, cell volume measurements and the fractional abundances of each cell population using non-linear least square regression. Grey dashed lines depict the change of intracellular metabolite concentrations relative to concentrations inferred for daughter cells (i.e. young cells at an age of 0 h). The change in ATP concentration is highlighted in red. Supplementary Fig. 2c shows the data for each metabolite in absolute units. **(b)** The growth (μ), metabolite uptake and production rates at various cell ages were obtained by measuring the evolution of cell count and extracellular metabolites (including produced carbon dioxide and consumed oxygen) and fitting the acquired data to an ordinary differential equation model. A positive value indicates metabolite production and a negative uptake. To assess the validity of the inference approach physiological rates were independently determined from unlabeled and streptavidin-labeled cell cultures (time point 0 h), consisting of predominantly young cells. The shading reflects the inverse of the relative uncertainty of the estimation (i.e. values which are depicted with a higher transparency are more uncertain).

Phenotypical metabolic changes are accompanied by drastic intracellular flux rearrangements

To infer the intracellular flux distributions from the acquired physiological data, we used a recently developed computational method (9). This method rests on a thermodynamic and stoichiometric model of cellular metabolism (as a function of metabolite concentration and metabolic flux) and was shown to yield predictions in good agreement with ^{13}C based metabolic flux analysis, while not relying on labelling data (9). The model consists of a mass balanced metabolic reaction network, including glycolysis, gluconeogenesis, tricarboxylic acid cycle, amino acid-, nucleotide-, sterol-synthesis and two reactions accounting for the NAD(P)H demand required for scavenging of reactive oxygen species (ROS). The reaction directionalities are constrained by the associated changes in Gibbs energy, and the Gibbs energy dissipated by the sum of all metabolic processes is balanced with the Gibbs energy exchanged with the environment through exchange processes (i.e. the production and consumption of extracellular metabolites). Using this model and regression analysis, we analysed the inferred metabolite concentrations (Fig. 2a) and physiological rates (Fig. 2b) (Supplementary Fig. 6). Subsequently, we assessed the solution space of the regression solution by minimizing the absolute sum of fluxes (16) to obtain the intracellular flux distributions during aging (Method 4).

The inferred intracellular flux rearrangements with age echo our findings from the extracellular physiology. Up until an age of 20 h the intracellular physiology depicted a fermentative phenotype with a low flux into the pentose phosphate pathway and a low flux in an incomplete tricarboxylic acid cycle as the majority of carbon was leaving glycolysis through the pyruvate decarboxylase towards ethanol. After 20 h, cells began to gradually shift towards a respiratory flux distribution, where an increasing proportion of the incoming carbon flux was directed into the pentose phosphate pathway and half of the carbon flux leaving the upper glycolysis going each towards glycerol excretion and through the lower glycolysis in the tricarboxylic acid cycle, while part of the carbon loss was compensated by the uptake of ethanol and pyruvate (Fig. 3).

Figure 3 | Redirection of intracellular metabolic fluxes during cellular aging. The flux distributions were obtained by minimizing the absolute sum of fluxes within the solution space of the regression analysis of the inferred intracellular metabolite concentrations and physiological rates. The thickness of the arrows corresponds to the absolute value of the fluxes, normalized to the glucose uptake rate. The grey dots show the intracellular metabolite concentrations inferred for cells of the respective age where the diameter corresponds to the natural logarithm of the respective concentration. Note, that this flux map does not show the complete model stoichiometry of the metabolic network.

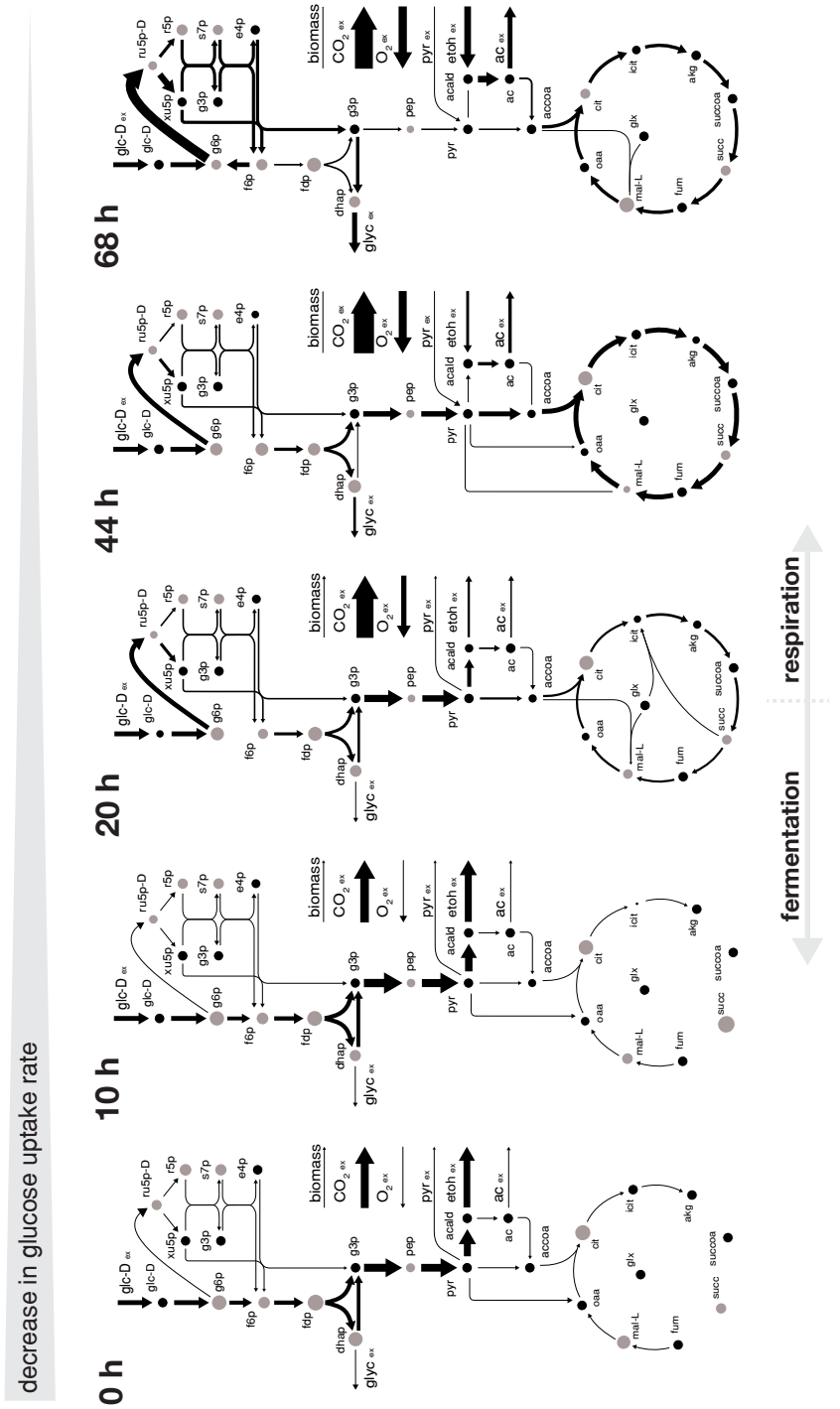
decrease in glucose uptake rate
0 h
10 h
20 h
44 h
68 h
fermentation
respiration
glc-D ex
glc-D
ru5p-D
r5p
xu5p
s7p
g3p
e4p
g6p
f6p
fdp
dhap
glyc ex
g3p
pep
pyr ex
acald
etoh ex
ac ex
ac
accoa
biomass
CO2 ex
O2 ex
pyr
oaa
cit
icit
akg
glx
mal-L
fum
succ
succoa

This switch in metabolic operation was accompanied by an increased redox nucleotide turnover (Fig. 4). Up until an age of 20 h, the majority of NADH was generated in glycolysis and regenerated through the alcohol dehydrogenase. After the switch to respiration, the tricarboxylic acid cycle became the major source of NADH, which in turn was regenerated in the respiratory chain. During the first 20 h, NADPH turnover was low but after the switch towards respiration NADPH was produced in the pentose phosphate pathway and through the aldehyde dehydrogenase. The increase in redox nucleotide turnover can be attributed to increased demands to combat emerging reactive oxygen species (ROS) (Fig. 4). Despite these dramatic changes in cofactor turnover, cells managed to maintain a constant NAD(P)H levels, as observed in age-spanning time-lapse analysis in single cells (Supplementary Fig. 7).

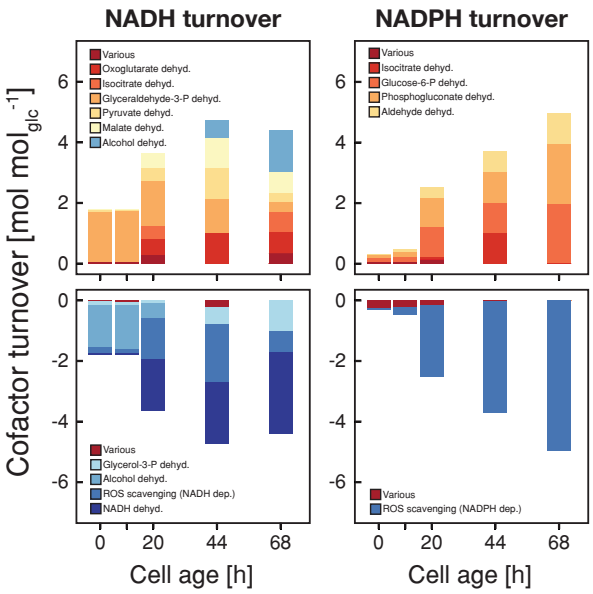

Figure 4 | The metabolic rearrangements with age are accompanied by shifts in redox cofactor turnover. The redox cofactor production and consumption rates (normalized by the respective glucose uptake rate) were obtained by minimizing the absolute sum of fluxes within the solution space of the regression analysis of the inferred intracellular metabolite concentrations and physiological rates. Reactions with a maximal turnover of $<0.5\,mol\,mol_{glc}^{-1}$ were combined and depicted as *various*. Note, that we did not enforce the emergence of ROS, however, the model could fit the experimental data the best by using cofactors for ROS scavenging.

DISCUSSION

Here, we complemented our earlier generated transcriptome and proteome account during the replicative aging of the budding yeast Saccharomyces cerevisiae, with the metabolic phenotype, inferred from cell ensemble measurements. Next to globally decreased metabolite levels, we found that cells shift with age from a fermentative towards a respiratory phenotype accompanied by a decrease in growth and glucose uptake rate. We hypothesize that the increase in cellular volume with age (cf. Supplementary Fig. 1) is responsible for the observed decrease in the volumetric (i.e. dry weight specific) substrate influx. Such decreased substrate influx will lead to decreased glycolytic fluxes, which

trigger a switch towards a respiratory metabolism (11). Increased respiratory activity (Fig. 2b and 3) could then lead to an increased generation of reactive oxygen species (17) necessitating an increase in redox cofactor turnover (Fig. 4) for ROS scavenging. This cascade of metabolic changes, likely induced by the non-homeostatic volume increases and the concomitant collapse in substrate uptake rate, might not only cause detrimental effects due to e.g. ROS production, but the reduced metabolic rates might also be responsible for the entry into senescence, as it was recently shown that sufficiently high enough metabolic rates are necessary for cells to pass cell cycle start (18).

METHODS

Method 1 | Strain and cultivation conditions

The haploid prototrophic *Saccharomyces cerevisiae* strain, YSBN6 (MATa, FY3 ho::HphMX4) (19), which is derived from S288c, was used in this study. All cultivations were performed using yeast nitrogen base (YNB) without amino acids (ForMedium, Norfolk, UK) supplemented with 2 % glucose at 30 °C and 300 rpm, unless indicated differently.

Column-based cultivation of yeast cells and sampling

To generate large quantities of aged yeast cells, necessary to perform bulk measurements, we used a method, in which cells were immobilized on iron beads and trapped inside a column (7). Briefly, cells were labelled with biotin and linked to streptavidin-coated iron beads. This iron bead bound cell culture was then grown in a column, equipped with an iron grid, in which the beads (and the cells attached to them) were trapped by a magnet. A continuous medium flow through the column washed out most emerging daughter cells and kept the mother cells in a constant, nutrient-rich environment. With the used flow rate of 170 mL h^{-1}, the glucose concentration stayed almost constant (only dropped from 21.7 to 20.1 g L^{-1}) and the concentration of major byproducts (pyruvate, succinate, glycerol, acetate and ethanol) never exceeded 1 g L^{-1}. Furthermore, the dissolved oxygen saturation never dropped below 75 %. The precise instrumental as well as experimental setup for the column-based cultivation and harvest can be found in (7).

As samples harvested from the column still resembled a mixture of mother, daughter and dead cells and any subsequent sorting step, aiming at an absolutely pure mother cell fraction would have inherently led to a distortion of the metabolic phenotype, we opted for an approach also followed in our previous study (7), to computationally infer the phenotype of each subpopulation. Specifically, we generated at each aging time point three samples with different proportions of mothers, daughter and dead cells (i.e. (1) from the column effluent, (2) from the column after an additional washing step, (3) from the washing solution

(in the following referred to as mix 1, 2 and 3)). After harvesting and before the respective analysis (and for the physiological characterization additionally at the end of the growth experiment), the cell count specific fractional abundance of each subpopulation in each sample was determined by flow cytometry and a combined dye-staining of propidium iodide and avidin – FITC. Later the metabolite concentrations and the cellular physiologies of each individual cell population (i.e. mother, daughter and dead cells) were mathematically inferred from data originating from the mixed samples and the determined fractional abundance.

Method 2 | Inference of intracellular metabolite concentrations

Regeneration

To allow the cells to recover from any possible stress during the sampling procedure, all samples were transferred in an Erlenmeyer flask containing 10 mL medium, adjusted to a cell density of $2x10^7$ cells mL^{-1} and incubated for 20 min at 30 °C and 300 rpm prior analysis.

Sample preparation

A sample of $3x10^7$ cells was taken from the Erlenmeyer flask and immediately quenched in 10 mL -40 °C methanol. The cells were separated from the organic solvent by centrifugation (5 min, 21'000 g, 4 °C), washed with 2 mL -40 °C methanol, separated again by centrifugation and stored at -80 °C. For the following analysis, the cell pellet was re-suspended in 900 µL -40 °C extraction buffer (methanol, acetonitrile and water, 4:4:2 v/v/v supplemented with 0.1 M formic acid) and an internal standard of ^{13}C-labeled metabolites was added to the extraction. This standard was obtained and quantified from exponentially growing cell cultures prior to the experiment (20). The extraction was agitated for 10 min at room temperature and thereafter centrifuged at maximum speed. The supernatant was transferred to a new vial and the cell pellet re-suspended in 900 µL -40 °C extraction buffer and the extraction procedure was repeated a second time. The supernatants from both steps were combined and centrifuged for 45 min at 4 °C and 21'000 g to remove any remaining non soluble parts. Thereafter, the supernatant was vacuum-dried at 45 °C for approximately 1.5 h and prior to the further analysis resolved in 200 µL water.

Measurement of intracellular metabolites

The extracted metabolite samples were analyzed using a UHPLC-MS/MS system. The chromatographic separation was performed on a Dionex Ultimate 3000 RS UHPLC (Dionex, Germering, Germany) equipped with a Waters Acquity UPLC HSS T3 ion pair column with precolumn (dimensions: 150 x 2.1 mm, particle size: 3 µm; Waters, Milford, MA, USA). The injection volume was 10 µL and the samples were permanently cooled at 4 °C. A binary solvent gradient was employed (0 min: 100 % A; 5 min: 100 % A 10 min: 98 % A; 11 min: 91 % A;

16 min: 91 % A; 18 min: 75 % A, 22 min: 75 % A; 22 min: 0 % A; 26 min: 0 % A; 26 min: 100 % A; 30 min: 100 % A) at a flow rate of 0.35 mL min^{-1} where solvent A was composed of 5 % methanol in water v/v supplemented with 10 mM tributylamine, 15 mM acetic acid and 1 mM 3,5-heptanedione and isopropanole as solvent B. The detection was done using multiple reaction monitoring (MRM) on a MDS Sciex API365 tandem mass spectrometer, upgraded to EP10+ (Ionics, Bolton, Ontario, Canada) and equipped with a Turbo-Ionspray source (MDS Sciex, Nieuwerkerk aan den Ijssel, Netherlands) with the following source parameter: NEB (nebulizing gas, N2): 12 a.u., CUR (curtain gas, N2): 12 a.u., CAD (collision activated dissociation gas): 4 a.u., IS (ion spray voltage): −4,500 V, TEM (temperature): 500 °C.

Mathematical inference of intracellular metabolite concentrations of mother and daughter cells using non-negative least squares regression

The concentrations of intracellular metabolites were determined from samples harvested after 10, 20, 44, and 68 h. The samples were measured in 6 replicates and the average of this replicates was used for the mathematical inference. To validate the interference approach we independently determined the intracellular metabolite concentrations of biotin labeled cells before loading them onto the column.

The in each sample (with n^{cell} cells) measured amount of metabolite, n^{meas}, contains metabolites originating from mother (*mo*) and daughter (*da*) cells. As dead cells were considered to be lysed and their metabolite content accordingly leaked into the medium, we assumed that their contribution to the total metabolite pool can be neglected. With taking the respective volumes of mother and daughter cells (Method 5 and Supplementary Fig. 1), and the fractional abundance of each population into account, the amount of substance of each metabolite in each cell is given by,

$$\frac{n_{i,j,k}^{meas}}{n_{j,k}^{cell}} = \alpha_{j,k} V_k^{mo} c_{i,k}^{mo} + \beta_{j,k} V^{da} c_i^{da} \quad \text{, Eq.1}$$

where $n_{i,j,k}^{meas}$ is the measured amount of substance (unit mol) of the metabolite i in the sample j at the aging time point k, $n_{j,k}^{cell}$ the total amount of cells in the respective sample, $\alpha_{j,k}$ and $\beta_{j,k}$ the cell count specific fractional abundance of mother and daughter cells, V_k^{mo} and V^{da} the cell volume (unit L $cell^{-1}$) of mother and daughter cells and $c_{i,k}^{mo}$ and c_i^{da} the metabolite concentration (unit M) in mother and daughter cells. Note that c_i^{da} and V^{da} are not indexed over the aging time points k, as we assumed that the daughter cell phenotype does not change over time (i.e. with proceeding mother cell age). To infer the intracellular metabolite concentrations c_k^{mo} and c^{da} from the measurements, n^{meas}, we formulated a non-linear least square regression problem of the form,

$$\min_x \left\| Ac - n \right\|_2^2, \quad c \geq 0 \qquad \text{, Eq.2}$$

where the matrix A contains all fractional volumes $\alpha_{j,k}\ V_k^{mo}$ and $\beta_{j,k}\ V^{da}$ in every sample j at every aging time point k, the vector c the unknown concentrations $c_{i,k}^{mo}$ and c_i^{da} of the metabolite i in mother and daughter cells at every aging time point k and the vector n all metabolite measurements, $n_{i,j,k}^{meas}$, normalized by the total amount of cells in the sample, $n_{j,k}^{cell}$, in every sample j at every aging time point k.

The regression problem in Eq. 2 was implemented in MATLAB (Release R2013, MathWorks, Inc., Massachusetts, USA) and the unknown metabolite concentrations, c, in mother and daughter cells were identified using the function "lsqnonneg". The uncertainty of the estimation was then determined by leave-one-out cross-validation, where we one-by-one removed data points from the set and repeated the estimation procedure (Supplementary Fig. 2).

Method 3 | Inference of growth, metabolite uptake and production rates

The physiological parameters (i.e. growth, metabolite uptake and production rates) were determined from two independent experimental campaigns. In campaign I, samples were harvested after 20, 44 and 68 h and in campaign II after 10, 20, 44, and 68 h where the samples from campaign II were split and analyzed in duplicates. The three data sets of both campaigns were combined for the inference. Additionally, we determined the physiologies of biotin labeled cells (referred to as '0 h') and unlabeled cells (referred to as 'unlabeled').

Batch cultivation conditions in minimal medium

The three samples obtained from the cultivation column (i.e. mix 1, 2 and 3) as well as the two reference samples (i.e. 0 h and unlabeled) were transferred each in a 250 mL Erlenmeyer flask (or RAMOS flasks) containing 25 mL medium, adjusted to a cell density of $2x10^7$ cell mL^{-1}, and incubated at 300 rpm and 30 °C.

Determination of cell dry weight from cell count

The cell count was measured every 20 min between 1 and 3 h after inoculation using a BD Accuri C6 flow cytometer (Becton, Dickinson and Company, Franklin Lakes, NJ). The samples were diluted with PBS at pH 7 to $< 10^6$ cells mL^{-1} and 20 µL sample were counted at 'medium' flow. The FSC-H thresholds was set to 80'000 in order to cut off most of the electronic noise. To correct the measured dry weight for the mass of iron beads in the sample, the iron beads were gated separately and counted as well. The data were analyzed using the Accuri CFlow Plus software.

Towards converting the measured cell counts to dry weight (biomass), we first determined the cell specific dry weight (i.e. the weight of one cell) of mother/dead, $m^{mo/de}$, and daughter cells, m^{da}. After 3 h, at the end of each batch cultivation, 20 mL of culture were filtered through a pre-weighed nitrocellulose filter with a pore size of 0.2 µm. The filter was washed once with distilled water,

dried at 80 °C for two days and afterwards weighed again. The total weight of iron beads attached to mother cells (here we assumed that one mother cell is attached to one iron bead (7)) and free beads, which was determined from the counted number of iron beads in the sample and the weight of one individual bead, was subtracted from the total dry weight of each sample. The bead weight had been determined to be 8.49×10^{-13} g per bead by filtration and weighting of a known amount of beads. Next, the cell specific dry weight of mother/dead and daughter cells was inferred from the measured population-average dry weight in the samples, m^{meas}, by following a similar approach as done for the intracellular metabolite concentrations. Specifically, we assumed that dead cells (i.e. died mother cells) and mother cells have the same dry mass and that the dry mass of newly formed daughter cells does not change over the aging time points. Taking the fractional abundances of each cell population into account, the measured cell specific dry mass in each sample is given as,

$$\frac{m_{j,k}^{meas}}{n_{j,k}^{cell}} = (\alpha_{j,k} + \gamma_{j,k}) m_k^{mo/de} + \beta_{j,k} m^{da} \quad \text{, Eq.3}$$

where $m_{j,k}^{meas}$ is the measured population-average dry mass (unit g) after 3 h cultivation in the sample j at the aging time point k, $n_{j,k}^{cell}$ the total amount of cells in the respective sample, $\alpha_{j,k}$ the cell count specific fraction of mother cells, $\gamma^{j,k}$ the cell count specific fraction of dead cells, $m_k^{mo/de}$ the cell specific dry mass (unit g) of mother or dead cells, $\beta_{j,k}$ the cell count specific fraction of daughter cells and m^{da} the cell specific dry mass (unit g) of daughter cells. Next, we formulated a least square regression problem of the form,

$$\min_x \left\| Am - n \right\|_2^2 \quad \text{, Eq.4}$$

where the matrix A contains all fractional abundances $\alpha_{j,k} + \gamma_{j,k}$ and $\beta_{j,k}$ in every sample j at every aging time point k, the vector m the unknown cell specific dry weights $m_k^{mo/de}$ and m^{da} at every aging time point k and the vector n all measured cell dry weights, $m_{j,k}^{meas}$, normalized by the total amount of cells in the sample, $n_{j,k}^{cell}$, in every sample j at every aging time point k. The regression problem in Eq. 4 was implemented in R (Release 3.2.0) and the unknown cell specific dry weights, m, of mother/dead and daughter cells were identified using the function "lm".

The inferred cell specific dry weights of mother/dead and daughter cells were then used to convert the measured cell counts to dry weight. At the beginning of each cultivation ($t = 0$) the total dry weight, $X_{t=0}$, is constituted of mother/dead and daughter cells, taking their fractional abundance into account, while in the following all new emerging cells are daughter cells. The total dry weight at every time t, X_t, is then given as,

$$X_{t,j,k} = \underbrace{(\alpha_{t=0,j,k} + \gamma_{t=0,j,k}) n_{t=0,j,k} m_k^{mo/de} + \beta_{t=0,j,k} n_{t=0,j,k} m^{da}}_{X_{t=0,j,k}} + (n_{t,j,k} - n_{t=0,j,k}) m^{da} \quad \text{, Eq. 5}$$

where $X_{t,j,k}$ is the dry weight of the mixed population sample j of the aging time point k at time t, $\alpha_{t=0,j,k} + \gamma_{t=0,j,k}$ and $\beta_{t=0,j,k}$ the cell count specific fractional abundances of mother/dead and daughter cells at the beginning of the cultivation, $n_{t=0,j,k}$ the cell count at the beginning of the cultivation and $n_{t,j,k}$ the cell count at the time t. Note that k refers to the cell age (i.e. aging time point) and t refers to the cultivation time at each aging time point (between 0 and 3 h).

Additionally, the inferred cell specific dry weights of mother/dead and daughter cells were used to convert the cell count specific fractional abundances, $\alpha_{j,k}$, $\beta_{j,k}$, and $\gamma_{j,k}$, in the dry mass specific fractional abundances of mother, daughter and dead cells, $\alpha_{j,k}^{dw}$, $\beta_{j,k}^{dw}$, and $\gamma_{j,k}^{dw}$, in every sample j at every aging time point k:

$$\alpha_{j,k}^{dw} = \frac{\alpha_{j,k} m_k^{mo/de}}{(\alpha_{j,k} + \gamma_{j,k}) m_k^{mo/de} + \beta_{j,k} m^{da}} \quad \text{, Eq. 6}$$

$$\beta_{j,k}^{dw} = \frac{\beta_{j,k} m_k^{mo/de}}{(\alpha_{j,k} + \gamma_{j,k}) m_k^{mo/de} + \beta_{j,k} m^{da}} \quad \text{, Eq. 7}$$

$$\gamma_{j,k}^{dw} = \frac{\gamma_{j,k} m_k^{mo/de}}{(\alpha_{j,k} + \gamma_{j,k}) m_k^{mo/de} + \beta_{j,k} m^{da}} \quad \text{. Eq. 8}$$

Determination of glucose and extracellular metabolite concentration

0.3 mL samples were taken every 20 min from 1 to 3 h after inoculation. To separate the cells from the medium, the samples were centrifuged at maximum speed for 3 min, the supernatant transferred onto a filter column (SpinX, pore size 0.22 µm), again centrifuged at maximum spend and the flow through was further analyzed. The glucose, pyruvate, glycerol, acetate and ethanol concentration was detected using an Agilent 1290 LC HPLC system equipped with a Hi-Plex H column and 5 mM H_2SO_4 as eluent at a constant flow rate of 0.6 mL min^{-1}. The injection volume was 10 µL and the column temperature was kept constant at 60 °C. Glucose, glycerol, ethanol and acetate were detected by refractive index and pyruvate by UV (constant wave length of 210 nm) and the respective concentrations were determined using an external standard with known concentrations. The data were analyzed using the Agilent Open Lab CDS software.

Determination of total consumed oxygen and produced carbon dioxide

The oxygen transfer rate (OTR) and carbon dioxide transfer rate (CTR) were determined from exhaust gas analysis using a respiration activity monitoring system (RAMOS) (13). The RAMOS measurement flask, containing 25 mL medium, was inoculated with $2x10^7$ cell mL^{-1} and the cultivation conditions were identical to the batch cultures used to determine the other physiological parameters. One RAMOS measurement cycle encompassed a 10 min measuring phase and a 20 min rinsing phase. The total consumption of oxygen and the production of carbon dioxide in a time interval were calculated from the mean of two consecutive OTR and CTR measurement cycles multiplied by the time.

Inference of growth, metabolite uptake and production rates of mother and daughter cells

To infer the physiological parameter of mother (*mo*), daughter (*da*) and dead (*de*) cells from the mixed population measurements, we formulated an ordinary differential equation model describing the dynamic change of biomass and extracellular metabolites during the 3 h cultivation in each sample. To this end, we assumed that the physiology of daughter cells stays constant over all aging time points and that within the 3 h cultivation the physiology of the mother cells stays constant. Finally, due to the short experiment time the evaporation of water and metabolites was neglected.

The total biomass in the sample is constituted of mother, dead and daughter cells and thus the differential mass balance can be formulated as,

$$0 = \frac{d}{dt}\alpha_{j,k}^{dw} + \frac{d}{dt}\beta_{j,k}^{dw} + \frac{d}{dt}\gamma_{j,k}^{dw} \quad \text{. Eq. 9}$$

Due to the short experiment time (3 h) compared to their life span (> 50 h), we assumed that the amount of initial mother and dead cells stays constant (i.e. no new mother cells emerge and no mother cell die during the experiment). Thus,

$$\frac{d}{dt}X_{j,k}^{mo} = \frac{d}{dt}(\alpha_{j,k}^{dw}X_{j,k}) = 0 \quad \text{, Eq. 10}$$

and

$$\frac{d}{dt}X_{j,k}^{de} = \frac{d}{dt}(\gamma_{j,k}^{dw}X_{j,k}) = 0 \quad \text{, Eq. 11}$$

where $X_{j,k}$ is the total biomass and $X_{j,k}^{mo}$ and $X_{j,k}^{de}$ the biomass of mother and dead cells in sample j at the aging time point k.

From Eq. 9, Eq. 10 and Eq. 11 follows that the change in total biomass is only due to the change in daughter cell biomass, $X_{j,k}^{da}$, which in turn can be either due to the emergence of new daughter cells originating from mother cells (i.e. budding

of mother cells) or originating from daughter cells (i.e. budding of daughter cells). Thus, the change of the total biomass is given as,

$$\frac{d}{dt}X_{j,k} = \frac{d}{dt}X_{j,k}^{da} = \frac{d}{dt}(\beta_{j,k}^{dw}X_{j,k}) = \mu_k^{mo}\alpha_{j,k}^{dw}X_{j,k} + \mu^{da}\beta_{j,k}^{dw}X_{j,k} \quad \text{, Eq. 12}$$

where μ_k^{mo} is the growth rate (unit h^{-1}) of mother cells and μ^{da} is the growth rate (unit h^{-1}) of daughter cells.

Reformulating the partial derivatives in Eq. 10 and Eq. 11 yields the change in dry mass specific fractional abundance of mother and dead cells as,

$$\frac{d}{dt}\alpha_{j,k}^{dw} = \frac{\alpha_{j,k}^{dw}}{X_{j,k}}\frac{d}{dt}X_{j,k} = -\alpha_{j,k}^{dw}(\alpha_{j,k}^{dw}\mu_k^{mo} + \beta_{j,k}^{dw}\mu^{da}) \quad \text{, Eq. 13}$$

and

$$\frac{d}{dt}\gamma_{j,k}^{dw} = \frac{\gamma_{j,k}^{dw}}{X_{j,k}}\frac{d}{dt}X_{j,k} = -\gamma_{j,k}^{dw}(\alpha_{j,k}^{dw}\mu_k^{mo} + \beta_{j,k}^{dw}\mu^{da}) \quad \text{, Eq. 14}$$

and plugging Eq. 13 and Eq. 14 in the differential biomass balance (Eq. 9) yields the change in fractional abundance of daughter cells due to budding of mother and daughter cells as,

$$\frac{d}{dt}\beta_{j,k}^{dw} = (\alpha_{j,k}^{dw} + \gamma_{j,k}^{dw})(\alpha_{j,k}^{dw}\mu_k^{mo} + \beta_{j,k}^{dw}\mu^{da}) \quad \text{. Eq. 15}$$

Next, the change in glucose concentration in the medium can be due to the uptake by mother and daughter cells as in,

$$\frac{d}{dt}c_{glc,j,k} = -X_{j,k}(\alpha_{j,k}^{dw}\underbrace{\frac{\mu_k^{mo}}{Y_{XS,k}^{mo}}}_{q_{S,k}^{mo}} + \beta_{j,k}^{dw}\underbrace{\frac{\mu^{da}}{Y_{XS}^{da}}}_{q_S^{da}}) \quad \text{, Eq. 16}$$

where $c_{glc,j,k}$ is the measured glucose concentration (unit g gCDW^{-1} h^{-1}) in sample j at the aging time point k, $q_{S,k}^{mo}$ and q_S^{da} the specific uptake rates of mother and daughter cells and $Y_{XS,k}^{mo}$ and Y_{XS}^{da} the biomass yields (unit g gCDW^{-1}) of mother and daughter cells.

In a similar way, the mass balance for oxygen, carbon dioxide and other fermentation products can be formulated:

$$\frac{d}{dt}c_{O_2,j,k} = -X_{j,k}(\alpha_{j,k}^{dw}\underbrace{Y_{O_2S,k}^{mo}\frac{\mu_k^{mo}}{Y_{XS,k}^{mo}}}_{q_{O_2,k}^{mo}} + \beta_{j,k}^{dw}\underbrace{Y_{O_2S}^{da}\frac{\mu^{da}}{Y_{XS}^{da}}}_{q_{O_2}^{da}}) \quad \text{, Eq. 17}$$

$$\frac{d}{dt}c_{P,j,k} = X_{j,k}(\alpha_{j,k}^{dw}\underbrace{Y_{PS,k}^{mo}\frac{\mu_k^{mo}}{Y_{XS,k}^{mo}}}_{q_{P,k}^{mo}} + \beta_{j,k}^{dw}\underbrace{Y_{PS}^{da}\frac{\mu^{da}}{Y_{XS}^{da}}}_{q_P^{da}}) \quad \text{, Eq. 18}$$

where $q_{O2,k}^{mo}$, q_{O2}^{da}, $q_{P,k}^{mo}$ and q_P^{da} are the biomass specific oxygen uptake and product (including carbon dioxide) excretion rates (unit g gCDW^{-1} h^{-1}) of mother and daughter cells at the aging time point k and $Y_{O2S,k}^{mo}$, Y_{O2S}^{da}, $Y_{PS,k}^{mo}$ and Y_{PS}^{da} the respective oxygen and product yields (unit g gCDW^{-1}) of mother and daughter cells.

To increase robustness in the estimation, we stated that the mother and daughter cell physiology needs to fulfill the carbon balance within a certain range.

$$0.5 \le \frac{\sum q_P^C}{q_S^C} \le 1.5 \quad \text{, Eq. 19}$$

where q_S^C and q_P^C are the specific carbon uptake and excretion rates (unit C-mol gCDW^{-1} h^{-1}) of mother and daughter cells.

All three datasets were combined into one parameter estimation problem subject to the Eq. 12 to 19. All parameters (including initial conditions) as well as the associated uncertainties were estimated using Maximum Likelihood estimation implemented in the software gPROMS ModelBuilder (Release 4.0, PSE software systems) with the MINLP solver SRQPD where a constant variance (error model) was assumed for all measurements.

Method 4 | Inference of intracellular metabolic fluxes

Computational model of cellular metabolism

To determine the intracellular fluxes at different cell ages from the inferred metabolite concentrations and physiologies, we made use of a recently published computational inference method (9). This method rests on a combined thermodynamic and stoichiometric network model of cellular operation, $M(v, \ln c) \le 0$ (Eq. 20), consisting of a mass balanced metabolic reaction network, in which the reaction directionalities are constraint by the associated changes in Gibbs energy – as a function of the metabolite concentrations c – through the 2nd law of thermodynamics. Additionally, the Gibbs energy, which is dissipated through metabolic operation (i.e. the sum of all metabolic processes, *MET*) is balanced with the Gibbs energy exchanged with the environment through exchange processes (i.e. the production and consumption of metabolites, *EXG*),

$$\{M(v,\ln c) \le 0\} \triangleq \left\{ \begin{array}{c} \sum_{j\in MET} S_{ij} v_j = v_{i\in EXG} \quad \forall i \\ \Delta_r G'(\ln c)_j v_j \le 0 \quad \forall j \in MET \\ \sum_{j\in MET} \Delta_r G'(\ln c)_j v_j = \sum_{i\in EXG} \Delta_f G'(\ln c)_i v_i \end{array} \right\} \quad \text{, Eq. 20}$$

where S_{ij} is the stoichiometric coefficient of the i^{th} reactant (i.e. metabolite) in reaction j, v_j the rate of the reaction j (i.e. the flux through this reaction), $\Delta_r G_j'(\ln c)$ the Gibbs energy of reaction of the metabolic process j and $\Delta_f G_i'(\ln c)$ the Gibbs energy of formation of the reactant i.

The published, and here used, model for *Saccharomyces cerevisiae* encompasses the metabolic processes of glycolysis, gluconeogenesis, tricarboxylic acid cycle, amino acid-, nucleotide-, sterol-synthesis and considers the processes' location in the cytosol, mitochondria and extracellular space. To account for cofactor turnover due to the combatting of reactive oxygen species, which is known to occur at high replicative ages (21), the model was extended by reactions describing the oxidation of NADH and NADPH through glutathione in the cytoplasm as well as the glutathione exchange (i.e. a sink and a source). This exchange does not represent any direct metabolic process but needed to be included since the glutathione metabolism is not part of this model.

```
nadh[c] + gthox[c] => nad[c] + (2) gthrd[c]
nadh[c] + gthox[c] => nad[c] + (2) gthrd[c]
          gthox[c] <=>
          gthrd[c] <=>
```

A more detailed description of this model and its implementation can be found in (9).

Regression analysis

Using this model and the inferred age-dependent metabolite concentrations and physiologies, we formulated a regression problem minimizing the weighted residual sum of squares, $rss(y)$ (Eq. 21). As data we used (i) the inferred yields, $\tilde{Y}_i^{(k)}$ ($i \in PY$ means physiological yield), (ii) the inferred metabolite concentrations $\tilde{c}_i^{(k)}$ ($i \in MC1 \cup i \in MC2$ means metabolite concentration set 1 or 2 (see below)), both of daughter and aged mother cells at a replicate age of 0, 10, 20, 44 and 68 h and (iii) standard Gibbs energies of reaction, $\Delta_r \tilde{G}_j'^o$. The later were determined (including uncertainty) using the component contribution method (22) and as this was not possible for all standard Gibbs energies, to prevent overfitting, the regression was regularized by the Lasso method (23).

To ensure the same thermodynamic reference state (i.e. the same standard Gibbs energies of reactions) in all experimental conditions, we bundled all datasets in on regression problem and indexed the model (Eq. 20) over the experimental conditions k.

$$\overline{rss}(y) = \frac{1}{\#n_Y}\sum_{k,i\in PY}\left(\frac{\frac{v_i^{(k)}}{v_{glc-D\_EX}^{(k)}} - \tilde{Y}_i^{(k)}}{\tilde{Y}_i^{(k),SE}}\right)^2 +$$

$$\frac{1}{\#n_c}\left[\sum_{k,i\in MC1}\left(\frac{e^{\ln c_{i[c]}^{(k)}} - \tilde{c}_i^{(k)}}{\tilde{c}_i^{(k),SE}}\right)^2 + \sum_{k,i\in MC2}\left(\frac{0.9e^{\ln c_{i[c]}^{(k)}} + 0.1e^{\ln c_{i[m]}^{(k)}} - \tilde{c}_i^{(k)}}{\tilde{c}_i^{(k),SE}}\right)^2\right] + \quad \text{, Eq. 21}$$

$$\frac{1}{\#n_{CCM}}\sum_{j\in CC}\left(\frac{\Delta_r G'^{o}_j - \Delta_r \tilde{G}'^{o}_j}{\Delta_r \tilde{G}'^{o,SE}_j}\right)^2 + \frac{0.05}{\#n_{unk}}\left|\Delta_r G'^{o}_j\right|$$

where $\#n_Y$ and $\#n_c$ are the number of inferred yields and metabolite concentrations, $\#n_{CCM}$ the number of standard Gibbs energies of reaction, which could be estimated by the component contribution method and $\#n_{unk}$ the number of reactions where no standard Gibbs energy of reaction could be calculated. The residuals were weighted by the respective prediction uncertainty, indicated by the superscript *SE*. Metabolites can occur in the cytoplasm and/or in the mitochondrial space (*MC1* means metabolites occurring in one compartment and *MC2* means metabolites occurring in two compartments). Thus, we stated that the sum of the metabolite concentrations in the respective compartments, weighted by the fractional compartmental volume (0.9 for the cytoplasm and 0.1 for the mitochondrial space), had to be equal to the inferred (cell-averaging) concentration. Last, to facilitate the convergence of the optimization and for an easy conversion of reaction rates to yields, the glucose uptake rate, $v_{glc\text{-}D\_EX}$, was constraint to a value of 1 mmol gCDW^{-1} h^{-1}.

The regression analysis was implemented in the mathematical programming system GAMS (GAMS Development Corporation. General Algebraic Modeling System (GAMS) Release 24.2.2. Washington, DC, USA).

Evaluation of the solution space

To obtain a picture of the intracellular flux distribution, we formulated the solution space, Ω^{reg} (Eq. 22), of the optimal regression solution, indicated by an *,

$$\Omega^{reg} = \left\{\begin{array}{l}(v^{(k)}, \ln c^{(k)}, \Delta_r G'^{o}) \mid M^{(k)}(v^{(k)}, \ln c^{(k)}, \Delta_r G'^{o}) \wedge \\ \left(\frac{v_i^{(k)}}{v_{glc-D\_EX}^{(k)}} = Y_i^{(k)*}\ \forall i \in PY\right) \wedge \left(\ln c_i^{(k)} = \ln c_i^{(k)}\ \forall i \in MC1\right) \wedge \\ \left(0.9e^{\ln c_{i[c]}^{(k)}} + 0.1e^{\ln c_{i[m]}^{(k)}} = 0.9e^{\ln c_{i[c]}^{(k)*}} + 0.1e^{\ln c_{i[m]}^{(k)*}}\ \forall i \in MC2\right) \wedge \\ \left(\Delta_r G'^{o} = \Delta_r G'^{o*}\right)\end{array}\right\} \quad \text{. Eq. 22}$$

Within this solution space we then minimized the 'absolute sum of fluxes',

$$\min\left\{\sum_j |v_j| : (v, \ln c) \in \Omega^{reg}\right\} \quad \text{. Eq. 23}$$

The optimization problem in Eq. 23 was implemented in the mathematical programming system GAMS (GAMS Development Corporation, General Algebraic Modeling System, Release 24.2.2., Washington, DC, USA).

Method 5 | Determination of NAD(P)H concentration, budding rate and cell size using single cell analysis

Microscopy

For microscopy experiments, cells from exponentially growing batch cultures were used to load a microfluidic device (24,25). Individual cells were monitored using an inverted fluorescence microscope (Eclipse Ti-E; Nikon) housed in an custom-made microscope incubator (Life Imaging Services GmbH) that retained temperature constant at 30 °C. During the experiment, cells were continuously fed with fresh medium. An LED-based excitation system (pE2; CoolLED) was used for illumination, and images were recorded using either an Andor 897 Ultra EX2 EM-CCD camera. NAD(P)H autofluorescence (excitation at 365 nm using a 357/44 nm filter and a 409 nm beam-splitter, 200 ms exposure time, 15 % light intensity, 435/40 nm emission, EM gain 1) was recorded every 60 min to minimize phototoxic effects, and brightfield images every 10 min to reliably track individual cells and determine their division times. A CSI S Fluor 40x Oil (NA = 1.3; Nikon) objective was used for NAD(P)H. Automated hardware (PFS; Nikon) was used for correction of axial focus fluctuations during imaging.

Image and data analysis

Cell segmentation for estimation of cell volume and fluorescence intensity took place in a semi-automated manner using the ImageJ plugin BudJ (26). For cell volume estimation, brightfield images captured with the 60x objective were used. Fluorescent intensity measurements were corrected for background fluorescence using the Rolling Ball Radius algorithm of ImageJ. For budding rate estimations on the basis of single-cells, the doubling time, t_d, (time from bud emergence to bud emergence) was measured for each cell in 60x brightfield images, and the budding rate for each doubling event ($\ln(2)\ t_d^{-1}$) was calculated.

Acknowledgements

We thank Silke Vedelaar for support during the metabolite extraction, Pieter Schmal and Alfredo Ramos from Process Systems Enterprise (PSE) for their support on the implementation of the ODE model. This work was carried out in

the Systems Biology Centre for Metabolism and Ageing (Groningen), which is funded by the Netherlands Organisation for Scientific Research (NWO) and the BE-BASIC consortium (BIOCapII).

REFERENCES

1. Kennedy BK, Austriaco NR, Guarente L. Daughter cells of Saccharomyces cerevisiae from old mothers display a reduced life span. J Cell Biol. 1994;127(6 Pt 2):1985–93.
2. Webb AE, Brunet A. FOXO transcription factors: key regulators of cellular quality control. Trends Biochem Sci. 2014;39(4):159–69.
3. Lagouge M, Larsson N-G. The role of mitochondrial DNA mutations and free radicals in disease and ageing. J Intern Med. 2013;273(6):529–43.
4. Barzilai N, Huffman DM, Muzumdar RH, Bartke A. The critical role of metabolic pathways in aging. Diabetes. 2012;61(6):1315–22.
5. McCormick MA, Kennedy BK. Genome-scale studies of aging: challenges and opportunities. Curr Genomics. 2012;13(7):500–7.
6. Eisenberg T, Büttner S, Kroemer G, Madeo F. The mitochondrial pathway in yeast apoptosis. Apoptosis. 2007;12(5):1011–23.
7. Janssens GE, Meinema AC, González J, Wolters JC, Schmidt A, Guryev V, et al. Protein biogenesis machinery is a driver of replicative aging in yeast. Elife. 2015;4:e08527.
8. Lin SS, Manchester JK, Gordon JI. Enhanced gluconeogenesis and increased energy storage as hallmarks of aging in Saccharomyces cerevisiae. J Biol Chem. 2001;276(38):36000–7.
9. Niebel B, Leupold S, Heinemann M. An upper limit in Gibbs energy dissipation governs cellular metabolism. Nat Metab. 2018;in press.
10. Ditzelmüller G, Wöhrer W, Kubicek CP, Röhr M. Nucleotide pools of growing, synchronized and stressed cultures of Saccharomyces cerevisiae. Arch Microbiol. 1983;135(1):63–7.
11. Huberts DHEW, Niebel B, Heinemann M. A flux-sensing mechanism could regulate the switch between respiration and fermentation. FEMS Yeast Res. 2012;12(2):118–28.
12. Litsios A, Ortega ÁD, Wit EC, Heinemann M. Metabolic-flux dependent regulation of microbial physiology. Curr Opin Microbiol. 2018;42:71–8.
13. Hansen S, Hariskos I, Luchterhand B, Büchs J. Development of a modified Respiration Activity Monitoring System for accurate and highly resolved measurement of respiration activity in shake flask fermentations. J Biol Eng. 2012;6(1):11.
14. Albertyn J, Hohmann S, Prior BA. Characterization of the osmotic-stress response inSaccharomyces cerevisiae: osmotic stress and glucose repression regulate glycerol-3-phosphate dehydrogenase independently. Curr Genet. 1994;25(1):12–8.
15. Giannattasio S, Guaragnella N, Ždralević M, Marra E. Molecular mechanisms of Saccharomyces cerevisiae stress adaptation and programmed cell death in response to acetic acid. Front Microbiol. 2013;4:33.
16. Holzhütter H-G. The principle of flux minimization and its application to estimate stationary fluxes in metabolic networks. Eur J Biochem. 2004;271(14):2905–22.
17. Drakulic T, Temple M, Guido R, Jarolim S, Breitenbach M, Attfield P, et al. Involvement of oxidative stress response genes in redox homeostasis, the level of reactive oxygen species, and ageing in. FEMS Yeast Res. 2005;5(12):1215–28.

18. Papagiannakis A, Niebel B, Wit EC, Heinemann M. Autonomous Metabolic Oscillations Robustly Gate the Early and Late Cell Cycle. Mol Cell. 2017;65(2):285–95.

19. Canelas AB, Harrison N, Fazio A, Zhang J, Pitkänen J-P, van den Brink J, et al. Integrated multilaboratory systems biology reveals differences in protein metabolism between two reference yeast strains. Nat Commun. 2010;1(9):145.

20. Wahl SA, Seifar RM, ten Pierick A, Ras C, van Dam JC, Heijnen JJ, et al. Quantitative Metabolomics Using ID-MS. In: Methods in molecular biology (Clifton, NJ). 2014. p. 91–105.

21. Ayer A, Gourlay CW, Dawes IW. Cellular redox homeostasis, reactive oxygen species and replicative ageing in Saccharomyces cerevisiae. FEMS Yeast Res. 2014;14(1):60–72.

22. Noor E, Haraldsdóttir HS, Milo R, Fleming RMT. Consistent estimation of Gibbs energy using component contributions. PLoS Comput Biol. 2013;9(7):e1003098.

23. Hastie TJ., Tibshirani R, Friedman J. The elements of statistical learning: data mining, inference, and prediction. 2011;

24. Lee SS, Avalos Vizcarra I, Huberts DHEW, Lee LP, Heinemann M. Whole lifespan microscopic observation of budding yeast aging through a microfluidic dissection platform. Proc Natl Acad Sci U S A. 2012;109(13):4916–20.

25. Huberts DHEW, Sik Lee S, Gonzáles J, Janssens GE, Vizcarra IA, Heinemann M. Construction and use of a microfluidic dissection platform for long-term imaging of cellular processes in budding yeast. Nat Protoc. 2013;8(6):1019–27.

26. Ferrezuelo F, Colomina N, Palmisano A, Garí E, Gallego C, Csikász-Nagy A, et al. The critical size is set at a single-cell level by growth rate to attain homeostasis and adaptation. Nat Commun. 2012;3(1):1012.

SUPPLEMENTARY FIGURES

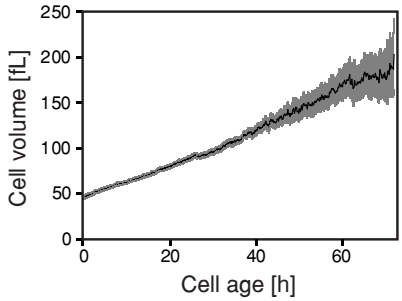

Supplementary Figure 1 | The cellular volume gradually increases with cellular age. Individual cells of *Saccharomyces cerevisiae* were tracked in a microfluidics device (24,25) and bright field images were recorded throughout their whole lifespan. The cellular volume was subsequently determined from the acquired microscopic data using the ImageJ plugin BudJ.

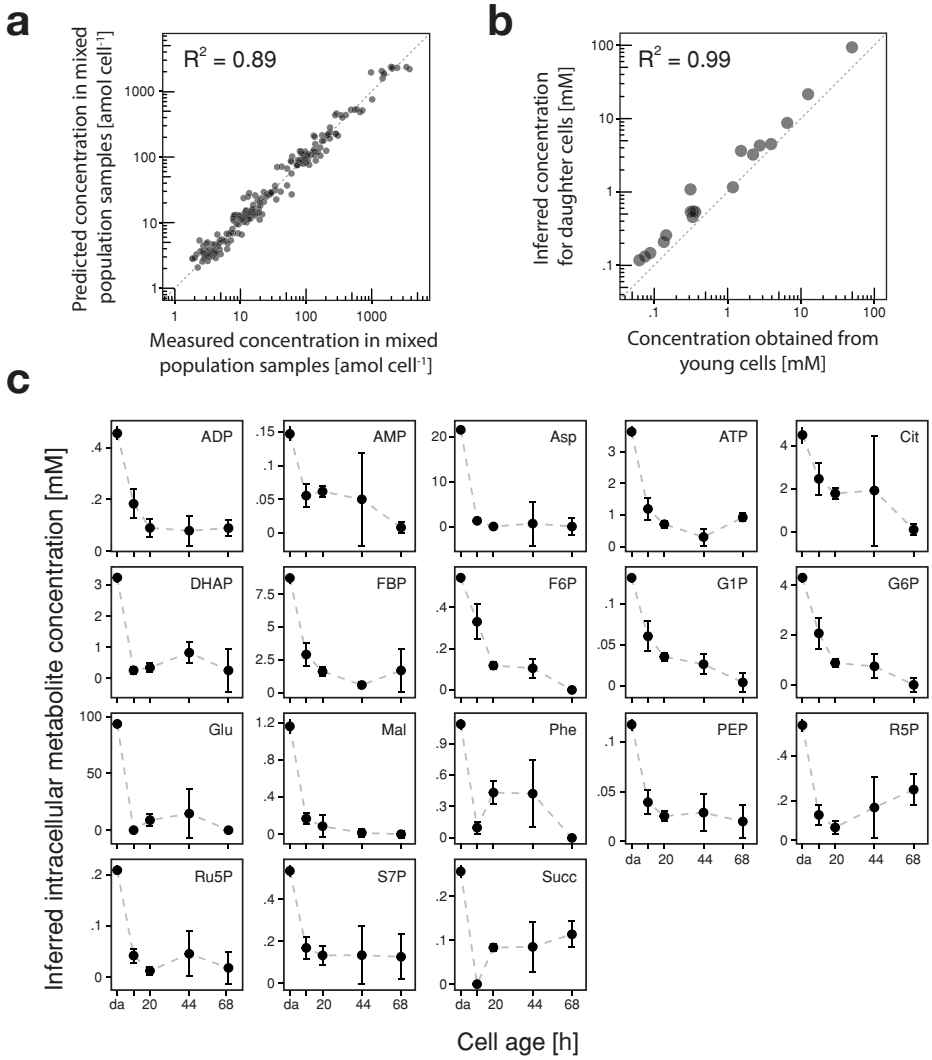

Supplementary Figure 2 | Inference of intracellular concentrations of 18 metabolites with cell age. (a) The intracellular concentration of 18 metabolites in daughter and aging mother cells was inferred from data obtained in various mixed population samples using non-negative least square regression where we obtained an excellent fit. **(b)** To confirm the validity of inference method for intracellular metabolite concentrations, we determined the metabolite concentration of young streptavidin-labeled cells and compared them to the inferred metabolite concentrations of daughter cells, which, by definition, should have the same phenotype. Here, we found a good consensus, confirming our approach. **(c)** We found a drastic decrease of metabolite concentrations with cell age (starting from young daughter cells (*da*)) of all 18 metabolites: adenosindiphosphat (ADP), adenosinmonophosphat (AMP), aspartic acid (Asp), adenosintriphosphat (ATP), citric acid (Cit), dihyroxy acetone phosphate (DHAP), fructose 1,6-bisphosphate (FBP), fructose-6-phosphate (F6P), glucose-1-phosphate (G1P), glucose-6-phosphate (G6P), glutamic acid (Glu), malic acid (Mal), phenylalanine (Phe), phosphoenolpyruvic acid (PEP), ribose-5-phosphate (R5P), ribulose-5-phosphate (Ru5P), sedoheptulose-7-phosphate (S7P) and succinic acid (Succ). The standard errors were determined by leave-one-out cross-validation, where we one-by-one removed data points from the set and repeated the estimation procedure.

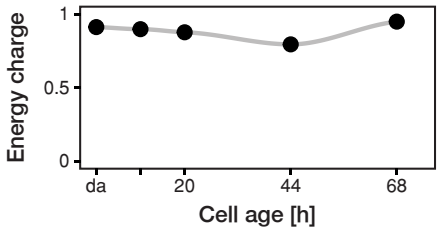

Supplementary Figure 3 | The energy charge remains constant with cell age. Despite the vast decrease of the inferred concentrations of all three adenosin nucleotides with cell age, the energy charge was maintained between 0.8 and 0.95, which corresponds to values of exponentially growing cultures (10).

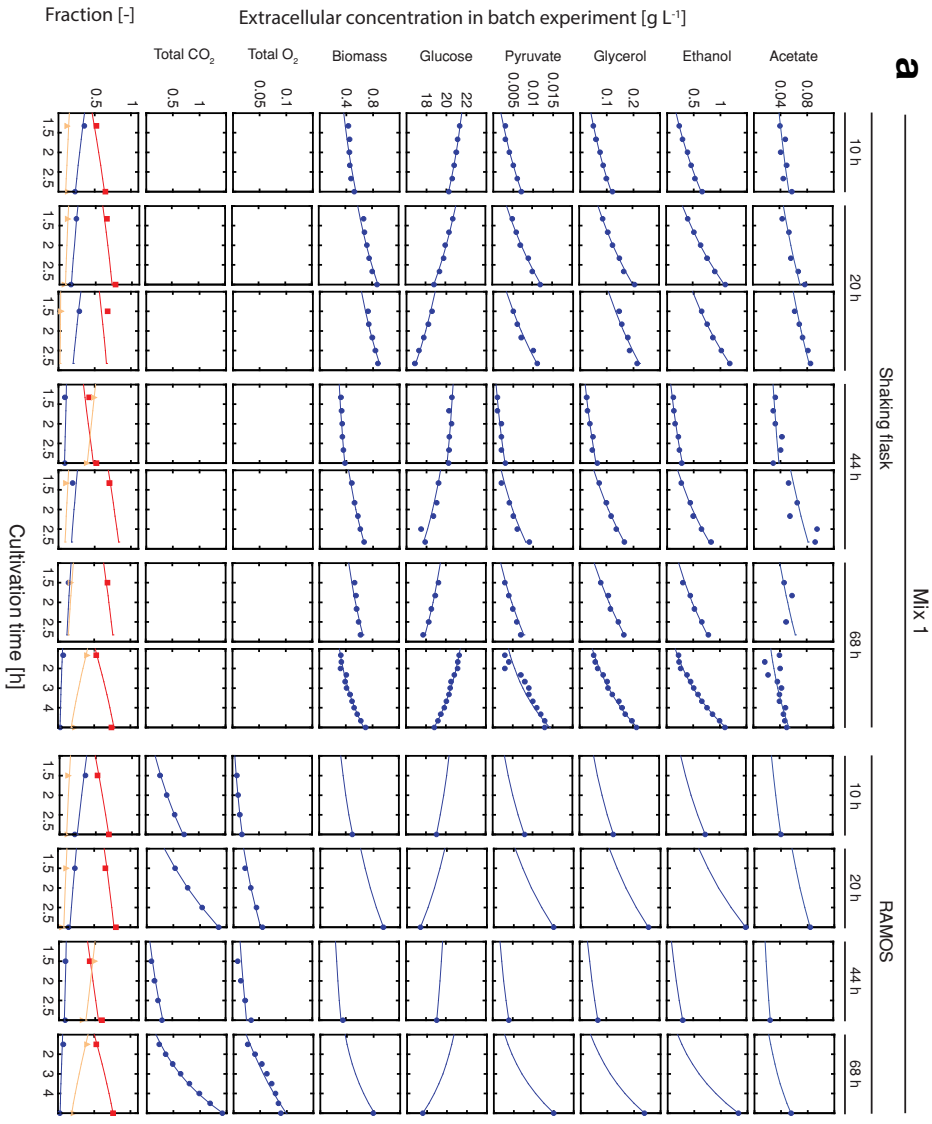
a
Mix 1
Shaking flask
RAMOS
10 h
20 h
44 h
68 h
Extracellular concentration in batch experiment [g L-1]
Acetate
Ethanol
Glycerol
Pyruvate
Glucose
Biomass
Total O2
Total CO2
Fraction [-]
Cultivation time [h]

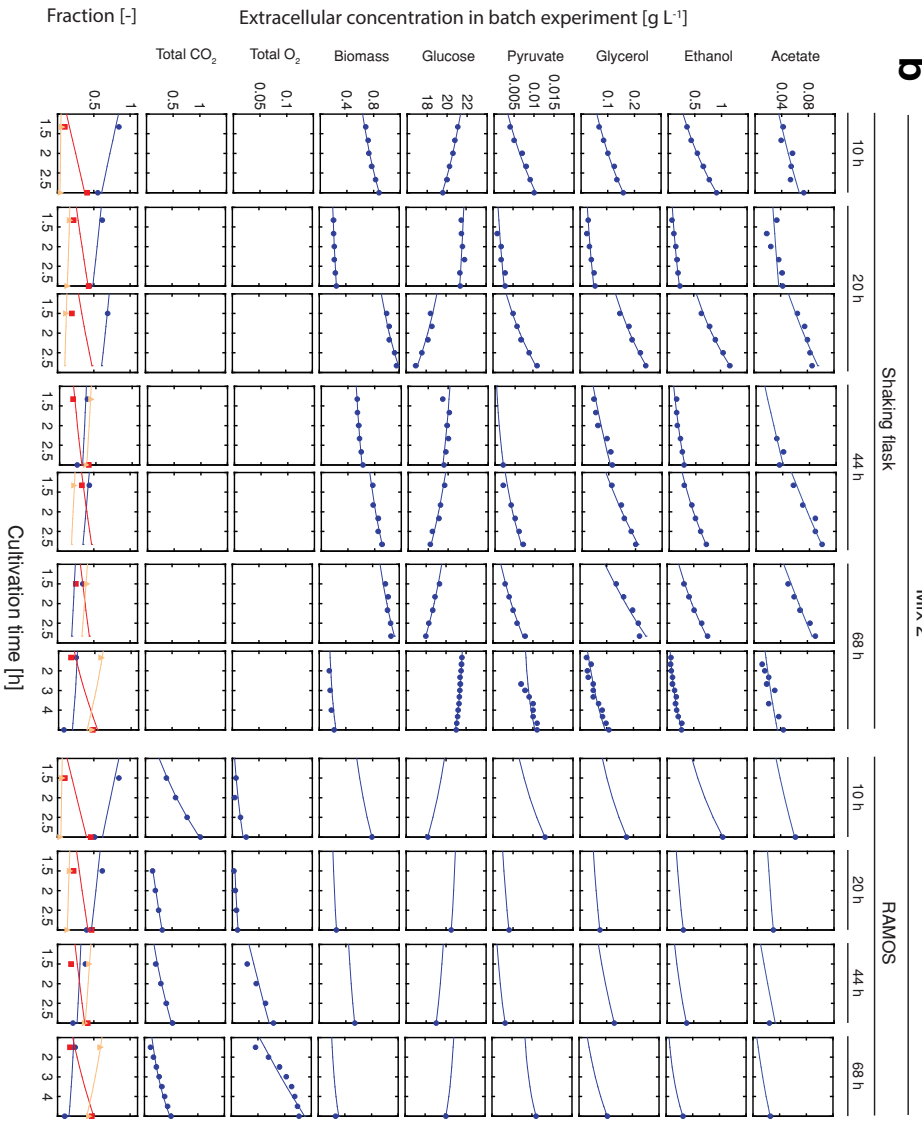
b
Mix 2
Shaking flask
RAMOS
10 h
20 h
44 h
68 h
Extracellular concentration in batch experiment [g L-1]
Acetate
Ethanol
Glycerol
Pyruvate
Glucose
Biomass
Total O2
Total CO2
Fraction [-]
Cultivation time [h]

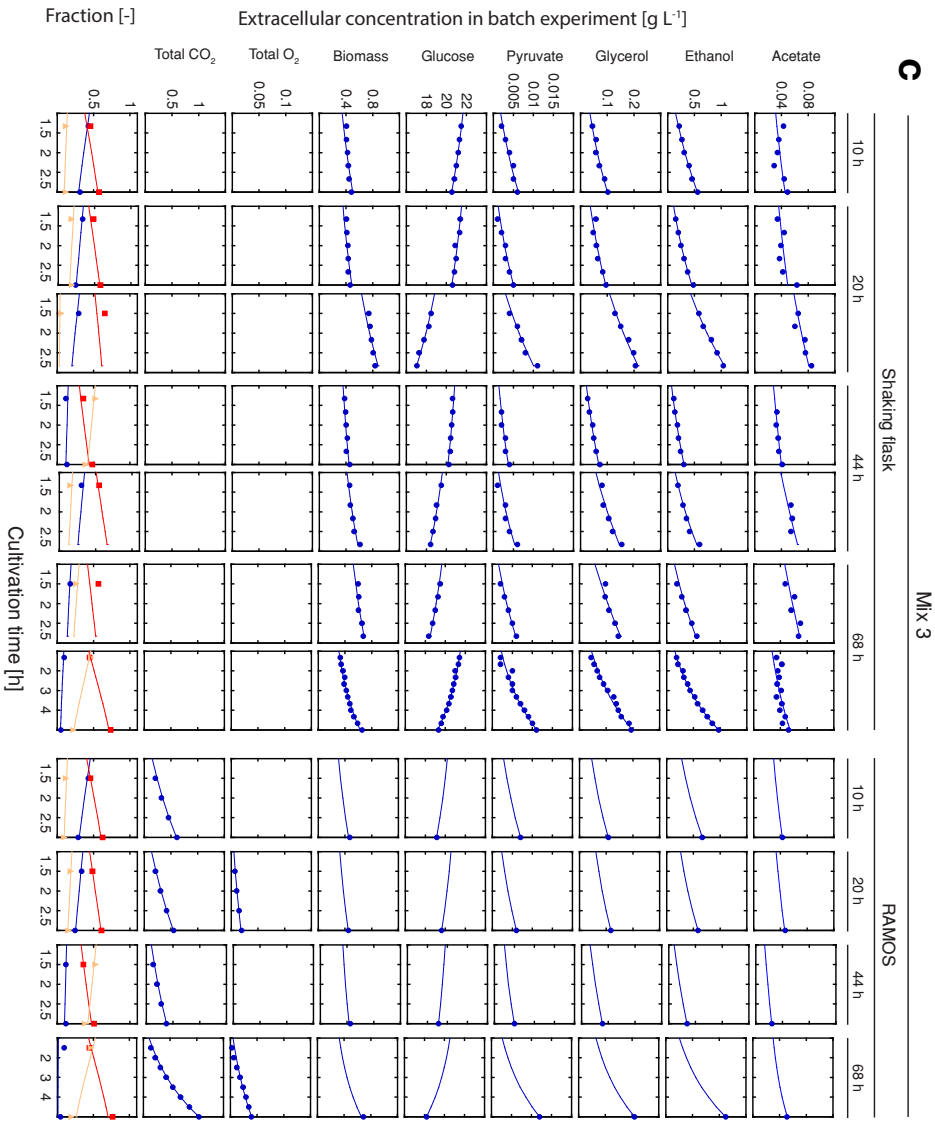

Supplementary Figure 4 | Inference of physiological parameters from dynamic changes in extracellular metabolites. At each time point (after 10, 20, 44 and 68 h), we measured the evolution of cell count (which was converted to dry weight (i.e. biomass)) and extracellular concentrations of acetate, ethanol, glycerol, pyruvate and glucose over a period of three hours in each harvested sample (i.e. mix 1 **(a)**, 2 **(b)** and 3**(c)**). The dry mass specific fractional abundance of each cell population was determined before and after that period. We used a second set of aliquots to measure the evolution of produced carbon dioxide and consumed oxygen using a Respiration Activity Monitoring System (RAMOS) (13). To infer the population-specific physiological rates from the mixed-population samples, we fitted the acquired dynamic data to an ordinary differential equation model, describing the changes of the biomass and extracellular metabolite concentrations in the samples, due to mother and daughter cell growth and their respective metabolism.

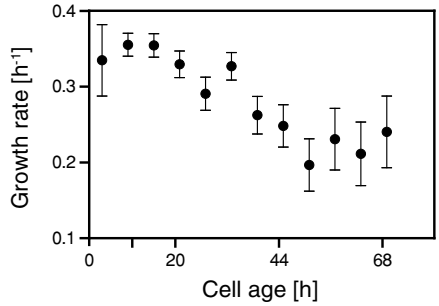

Supplementary Figure 5 | The decreasing growth rate was confirmed using single cell analysis. The decreasing growth rate inferred with cell age was confirmed using microfluidics and microscopy. Cells from an exponentially growing batch culture were loaded onto a microfluidics device and monitored for > 70 h. The doubling time (time from bud emergence to next bud emergence) was measured for each cell in bright-field images, and the growth rate for each doubling event ($\ln(2)\ t_d^{-1}$) was calculated. Growth rates within 6 hours windows were averaged. Note, that the growth rate in Fig. 2b was inferred from the increase of biomass in the culture while here the growth rate is determined from the budding rate of individual cells. Because of the prolonged G1 phase of newborn cells, deviations in the absolute value are possible. Both methods, however, show a decrease in growth rate.

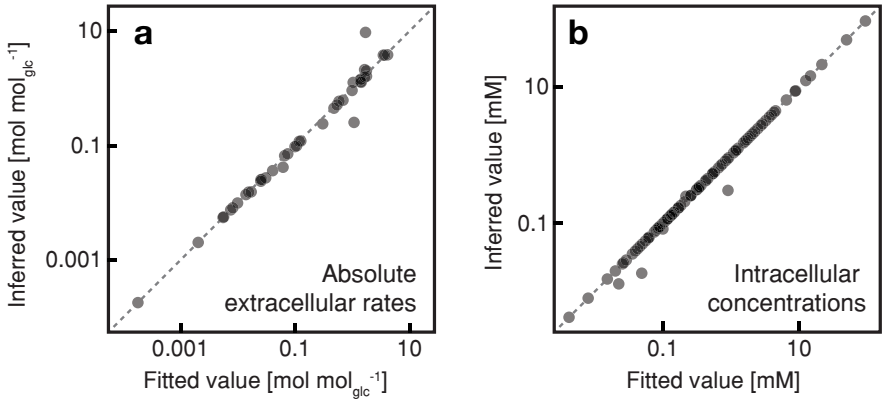

Supplementary Figure 6 | Results of the regression analysis using the combined thermodynamic and stoichiometric metabolic mode. The inferred extracellular metabolic rates (normalized by the respective glucose uptake rate) and intracellular metabolite concentrations of mother cell at an age of 0, 10, 20, 44 and 68 h were analyzed using regression analysis and a combined thermodynamic and stoichiometric metabolic network model. Fitted values from this regression analysis versus inferred values; **(a)** extracellular rates and **(b)** intracellular metabolite concentrations.

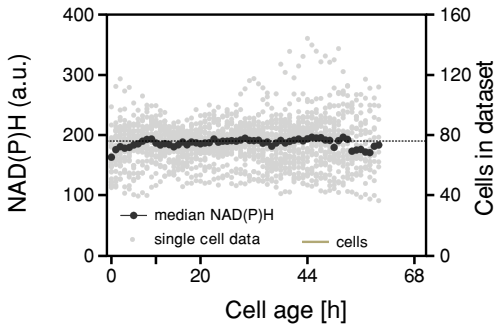

Supplementary Figure 7 | The intracellular NAD(P)H concentration remains constant with cell age. Individual cells of *Saccharomyces cerevisiae* were tracked in a microfluidics device and fluorescence images were recorded throughout their whole lifespan. The NAD(P)H concentration was inferred from the acquired autofluorescence (18).